Clim Dyn (2015) 44:133–146
DOI 10.1007/s00382-014-2233-2

Why the twenty-first century tropical Pacific trend pattern cannot significantly influence ENSO amplitude?

Soon-Il An · Jung Choi

Received: 10 May 2013 / Accepted: 29 June 2014 / Published online: 10 July 2014

Abstract Although the climate is highly expected to change due to global warming, it is unclear whether the El Nino-Southern Oscillation (ENSO) will be more or less active in the future. One may argue that this uncertainty is due to the intrinsic uncertainties in current climate models or the strong natural long-term modulation of ENSO. Here, we propose that the global warming trend cannot significantly modify ENSO amplitude due to weak feedback between the global warming induced tropical climate change and ENSO. By analyzing Coupled Model Intercomparison Project Phase 5 and observation data, we found that the zonal dipole pattern of sea surface temperature [SST; warming in the eastern Pacific and cooling in the western Pacific or vice versa; 'Pacific zonal mode' (PZM)] is highly correlated to change in ENSO amplitude. Additionally, this PZM is commonly identified in control experiments (pre-industrial conditions), twentieth century observations, and twenty-first century scenario experiments [representative concentration pathways 4.5 and 8.5 W m^{-2} (RCP 4.5, 8.5)]. PZM provides favorable conditions for the intensification of ENSO by strengthening air–sea coupling and modifying ENSO pattern. On the other hand, the twenty-first century SST trend pattern, which is different from PZM, is not favorable towards changing ENSO amplitude. Furthermore, we performed an intermediate ocean–atmosphere coupled model simulations, in which the SST trend pattern and PZM are imposed as an external anomalous heat flux or prescribed as a basic state. It was concluded that the SST trend pattern forcing insignificantly changes ENSO amplitude, and the PZM forcing intensifies ENSO amplitude.

Keywords ENSO · Global warming · Amplitude modulation · Pacific zonal mode

S.-I. An (✉)
Department of Atmospheric Sciences, Yonsei University, Seoul 120-749, Korea
e-mail: sian@yonsei.ac.kr

J. Choi
School of Earth and Environmental Sciences, Seoul National University, Seoul, Korea

1 Introduction

The El Nino-Southern Oscillation (ENSO) is the abnormal climate condition of SST over the tropical eastern-to-central Pacific. It is one of the strongest interannual phenomena on the Earth. During an ENSO event (i.e., El Nino and La Nina), the tropical eastern Pacific SST, which usually has the lowest temperature along the equatorial ocean band, reaches temperatures as high as those of the tropical western Pacific sea surface and as low as the temperature associated with complete surface outcropping of the thermocline (about 20 °C; An and Jin 2004; An 2009). The tropical western Pacific surface is a 'warm pool' that frequently records the radiative-convective equilibrium temperature (over 30 °C; Waliser and Graham 1993). These theoretical upper and lower limits of ENSO amplitude were referred to as maximum potential intensity (MPI; An and Jin 2004).

The increasing backward terrestrial radiation due to increases in greenhouse gases leads to a higher radiative-convective equilibrium temperature, i.e., pushing up the upper limit of El Nino (Kim and An 2011). Oceanic subsurface warming (e.g., thermocline adjustment) due to global warming may reduce the lower limit of La Nina. However, climate model scenario simulations of future greenhouse warming showed that the surface temperature over the cold tongue increases more than subsurface ocean temperature

at about 100 m depth (e.g., Timmermann et al. 1999; An et al. 2008). This expands the lower limit of the MPI. Therefore, the future MPI is expected to be larger, possibly indicating larger ENSO amplitude. Although MPIs of each model in the same experiment are mostly enhanced (e.g., An et al. 2008), amplitude changes in ENSO in future scenario experiments are statistically insignificant (Stevenson 2012) as well as model- and scenario-dependent (Meehl et al. 2007; Guilyardi et al. 2012; Kim and Yu 2012; Stevenson et al. 2012; Christensen et al. 2013). In general, climate warming increases the MPI, thereby increasing the potential range of ENSO amplitude; however, ENSO amplitude is not simply proportional to the MPI as seen in Coupled Model Intercomparison Project (CMIP).

Although the MPI constrains the range of ENSO amplitude, the actual fluctuation of ENSO is determined by various feedback and atmospheric stochastic process. These are mainly governed by large-scale dynamical and thermodynamical air–sea interactions (e.g., Neelin et al. 1998). Recently, Jin et al. (2006) introduced a linear coupled-stability index for ENSO known as the Bjerknes stability (BJ) index. Kim and Jin (2011) later showed a significant relationship between ENSO amplitude and the BJ index. The BJ index is determined by the mean state and the sensitivity in the inter-response between atmosphere and ocean such as atmospheric heating driven by changes in the SST, or ocean currents driven by surface wind stresses. The inter-response sensitivities can be modified by the mean state as well. Accordingly, changes in the mean state due to climate forcing influence ENSO amplitude, regardless of its statistical significance. Ample evidence of the dependency of ENSO amplitude on the mean state has been exhibited. As a result, it was suggested that the enhanced ENSO variability that occurred between the pre-1980s and the post-1980s was related to changes in the mean climate of the tropical Pacific such as the mean surface wind and upwelling (An and Wang 2000) or the mean thermocline (Fedorov and Philander 2000) or both (An and Jin 2000; Kim and An 2011). However, it is uncertain to what extent global warming modifies ENSO amplitude due to the uncertainty of the future state of the tropical Pacific mean state (e.g., Collins et al. 2010), the strong decadal-to-centennial modulation of ENSO through the internal process (Wittenberg 2009, 2014), and the complexity in the sensitivities of ENSO to changes in the mean state (e.g., Yu and Kim 2010; Kim and Yu 2012; Borlace et al. 2013). Moreover, it is questionable as to whether ENSO amplitude is sensitive to the climate state change associated with global warming.

To answer the question as to whether a change in ENSO amplitude associated with global warming is beyond that of natural change, we measure the range of the natural modulation of ENSO amplitude. Here, the natural modulation range of ENSO amplitude was computed using pre-industrial (PI) simulations (or a control simulation) because the PI simulation has no time-varying external climate forcing. The amplitude modulation of ENSO is defined as the standard deviation of the 11-year running standard deviation of the Nino-3 index. Although ENSO amplitude could be modulated in the centennial time scale, the decadal-to-interdecadal time scale modulation is thus far the most reliable. The 2,000-year simulation of GFDL CM2.1 also shows dominant interdecadal fluctuation of ENSO amplitude than the longer time scale (Wittenberg 2009). Thus we focus on the fluctuations within interdecadal time scale. Note that the wider window for running standard deviation decreases the range and the narrow window has the opposite effect.

To compare the internal modulation range of ENSO amplitude to the anthropogenic effect on ENSO amplitude change, the change in the amplitude of ENSO associated with global warming is defined as the difference in the standard deviation of Nino-3 SSTA index (5°S–5°N, 150°–90°W) between the PI run and RCP run. For the RCP run, we use 95 years of data from 2006 to 2100 after removing linear trends. The range of the long-term natural modulation of ENSO amplitude is 0.1–0.3 K and is highly depending on the model, while the change in the amplitude of ENSO associated with global warming is 0–0.8 K and is strongly scattered (Fig. 1). Sixteen of the 31 models recorded that ENSO amplitude change associated with global warming is beyond the 50 % probability range of the natural modulation of ENSO amplitude. Four models are out of a 90 % probability range. Among these, only one model recorded a decrease in ENSO amplitude, while the others recorded an increase in ENSO amplitude. Approximately 10 % of Coupled Model Intercomparison Project Phase 5 (CMIP5) models show a somewhat significant increase in ENSO amplitude; others showed insignificant (or low chance) change in ENSO amplitude associated with global warming. On the whole, a 10 % chance is not sufficient to conclude that ENSO amplitude will increase due to global warming. The reason the change in ENSO amplitude due to global warming is less significant may be uncertainty in the internal processes of ENSO (Wittenberg 2009). However, in this study, we focus on the dynamical relationships between the change in mean state and ENSO.

By changing the mean climate state, we addressed how and to what extent climate warming influences ENSO amplitude. In Sect. 2, we introduce the CGCM output utilized and an intermediate coupled model (ICM). The mean patterns that are associated with ENSO amplitude are identified using the undisturbed climate forcing experiment in Sect. 3. In Sect. 4, we analyze the mean patterns associated with future global warming to determine whether they resemble patterns associated with ENSO amplitude in the undisturbed climate forcing experiment. To further verify

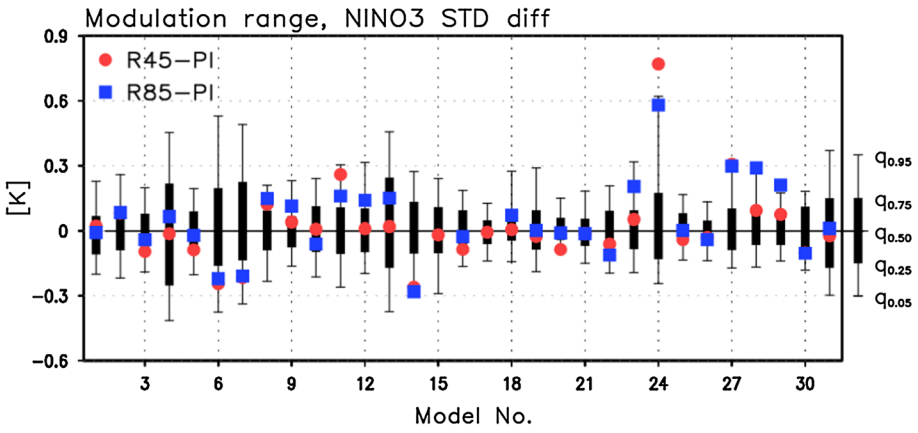

Fig. 1 Percentiles based on the standard deviation of 11 years running standard deviation of the Nino-3 index (5°S–5°N, 150°–90°W) obtained from the control experiment (PI setting) of CMIP5 (*bar*). *Thick* and *thin bars* indicate the 50 and 90 % probability range, respectively. *Circular* (*rectangular*) marks indicate the difference between the standard deviation of the Nino-3 index from RCP4.5 (RCP8.5) and that from the control experiment of CMIP5. The linear trend was removed prior to computation. The model numbers in the axis of abscissa are matched to Table 1

the previous findings, in Sect. 5, we performed an intermediate atmosphere–ocean coupled model experiment in which the mean patterns associated with ENSO amplitude are altered and those associated with global warming are externally adapted. A summary and discussion are included in Sect. 6.

2 Data and model

2.1 Data

2.1.1 Observation and reanalysis of data

In this study, four historical reanalysis SST datasets are used: (1) the Extended Reconstructed Sea Surface Temperature (ERSST) dataset, version 3 (Smith and Reynolds, 2004), (2) the extended Kaplan SST (Kaplan SST), version 2 (Kaplan et al. 1998), (3) the Hadley Centre Sea Ice and Sea Surface Temperature (HadISST) dataset, version 1 (Rayner et al., 2003), and (4) the Simple Ocean Data Assimilation (SODA) reanalysis dataset, version 2.2.4 (Carton and Giese 2008). The SODA reanalysis project reconstructs historical ocean climate variability over space and time scales similar to atmospheric reanalysis projects. Each dataset covers the periods of January 1951–November 2012 (ERSST, Kaplan SST), January 1951–September 2012 (HadISST), and January 1951–December 2008 (SODA). Their horizontal grids are interpolated onto a uniform 2° × 2° grid. Anomalies are defined as departure from the 1951–2011 climatological values for each month. All data are linearly detrended before statistics are calculated, which might be associated with a global warming trend.

2.1.2 CMIP5

General information about the coupled general circulation models (CGCMs) used in this study is summarized in Table 1, which consists of 31 CGCMs from phase 5 of the CMIP (Taylor et al. 2012). Three types of simulations were used: PI control and two future projection simulations forced with specified concentrations referred to as RCPs. Pre-industrial simulation has quasi-equilibrium integration, which has no time-varying external climate forcing. All models selected for PI simulation were integrated for more than 100 years. Furthermore, we select two RCP simulations for future climate analysis: a high emissions scenario (RCP8.5) and a midrange mitigation emissions scenario (RCP4.5). The labels for the RCPs provide a rough estimate of the radiative forcing in the year 2100 relative to PI conditions (Taylor et al. 2012). The integration periods are 95 years during 2006–2100 in both RCP runs. Note that the two CGCMs (GISS-E2-H-CC and GISS-E2-R-CC) are excluded from the RCP8.5 run. All model outputs are interpolated onto a uniform 2° × 2°grid.

2.2 Intermediate coupled model

The ICM is basically the same as Zebiak and Cane's (1987) model, which has been used to understand and predict ENSO. The atmosphere model of ICM is a steady state, linear, shallow-water system with an equatorial beta-plane assumption. This represents the baroclinic structure of a tropical atmosphere. Atmospheric forcing, which is mainly the latent heat releasing in the middle atmosphere due to convection, is controlled by the anomalous surface evaporation associated with change in the SST anomaly

Table 1 Model descriptions

No.	Models	Institution	Resolution	PI (years)
1	ACCESS1-0	CSIRO-BOM/Australia	192 × 145	250
2	ACCESS1-3	CSIRO-BOM/Australia	192 × 145	500
3	BCC-CSM1-1	BCC/China	128 × 64	500
4	BNU-ESM	BNU/China	128 × 64	550
5	CanESM2	CCCma/Canada	128 × 64	690
6	CCSM4	NCAR/USA	288 × 192	500
7	CESM1-BGC	NSF-DOE-NCAR/USA	288 × 192	500
8	CNRM-CM5	CNRM-CERFACS/France	256 × 128	850
9	CSIRO-Mk3.6	CSIRO-QCCCE/Australia	192 × 96	500
10	FGOALS-G2	LASG-CESS/China	128 × 60	700
11	GFDL-CM3	NOAA GFDL/USA	144 × 90	500
12	GFDL-ESM2G	NOAA GFDL/USA	144 × 90	500
13	GFDL-ESM2 M	NOAA GFDL/USA	144 × 90	500
14	GISS-E2-H	NASA-GISS/USA	144 × 90	240
15	GISS-E2-H-CC	NASA-GISS/USA	144 × 90	250
16	GISS-E2-R	NASA-GISS/USA	144 × 90	500
17	GISS-E2-R-CC	NASA-GISS/USA	144 × 90	250
18	HadGEM2-CC	MOHC/UK	192 × 145	240
19	HadGEM2-ES	MOHC/UK	192 × 145	475
20	INMCM4	INM/Russia	180 × 120	500
21	IPSL-CM5A-LR	IPSL/France	96 × 96	430
22	IPSL-CM5A-MR	IPSL/France	144 × 143	300
23	IPSL-CM5B-LR	IPSL/France	96 × 96	300
24	MIROC5	MIROC/Japan	256 × 128	670
25	MIROC-ESM	MIROC/Japan	128 × 64	530
26	MIROC-ESM-CHEM	MIROC/Japan	128 × 64	255
27	MPI-ESM-LR	MPI-M/Germany	192 × 96	900
28	MPI-ESM-MR	MPI-M/Germany	192 × 96	845
29	MRI-CGCM3	MRI/Japan	320 × 160	500
30	NorESM1-M	NCC/Norway	144 × 96	100
31	NorESM1-ME	NCC/Norway	144 × 96	250

PI (years) indicates the integration periods of the PI runs

The integration period is 95 years for both RCP runs (2006–2100)

and the moisture convergence feedback due to the interactive change with the lower level convergence. The ocean model is composed of the fixed-depth mixed layer, which determines the SST anomalies and surface horizonal currents, and the upper dynamic layer, which determines the thermocline depth. The motions in the dynamic layer are described by a linear shallow-water equation forced by the surface wind stress. The SST is determined by the horizontal advection in the mixed layer, vertical advection by the upwelling, and a comprehensive surface cooling (i.e., Newtonian cooling). The climatological basic states are prescribed, and thus we can measure the model's sensitivity to changes in basic states. Note that ICM has intrinsically nonlinear components, and thus the sensitivity can be influenced by the nonlinearity. Nevertheless, it is known that the variability and skewness (a measure of ENSO nonlinearity; An 2009) changes in the same direction (e.g., An et al. 2005). Therefore, the nonlinear process of ICM may not significantly influence the main conclusion.

3 ENSO amplitude modulation through internal processes

It may not be easily answered as to what controls the ENSO amplitude. Theoretically, the growth rate of a prototype ENSO model is related to various feedback processes (Jin 1997), but the intrinsic feedback processes are very complicated. Therefore, instead of considering each feedback process separately, we compute the regression pattern associated with ENSO amplitude, which provides a comprehensive feature. The PI experiments are utilized to identify patterns associated with ENSO amplitude change due to natural variation. Here, two indices are used: the ENSO index and the ENSO amplitude index (actually the decadal-modulation index of ENSO amplitude). To define the ENSO index, we apply the empirical orthogonal function (EOF) analysis to the tropical Pacific SST anomalies obtained from the PI experiment. The normalized first EOF principal component (PC) time series is then defined as the ENSO index. We characterize the ENSO amplitude index, which is referred to as the N3var index. The N3var index is computed using the interannual (2–7 years) wavelet variance of the Nino-3 SST anomaly as described in Torrence and Webster (1998).

The regression patterns of tropical Pacific SST anomalies are computed against the ENSO index and the normalized N3var index of each CMIP5 model. An ensemble-average with equal weighting is then taken. The regression patterns of the equatorial-band average (5°S–5°N) and the tropical Pacific SST anomaly against the ENSO index represent the conventional El Nino pattern, namely, the maximum loading over the equatorial eastern Pacific. The regressions from each model converge well to the ensemble mean curve (Fig. 2a, b). On the other hand, the regression pattern against the ENSO amplitude index (Fig. 2c, d) shows a zonal-dipole pattern, where the positive and negative centers are located at the tropical eastern Pacific and tropical western Pacific, respectively [hereafter referred to as the Pacific zonal mode (PZM)]. The regression lines from each model are diverse compared with the regression against the ENSO index.

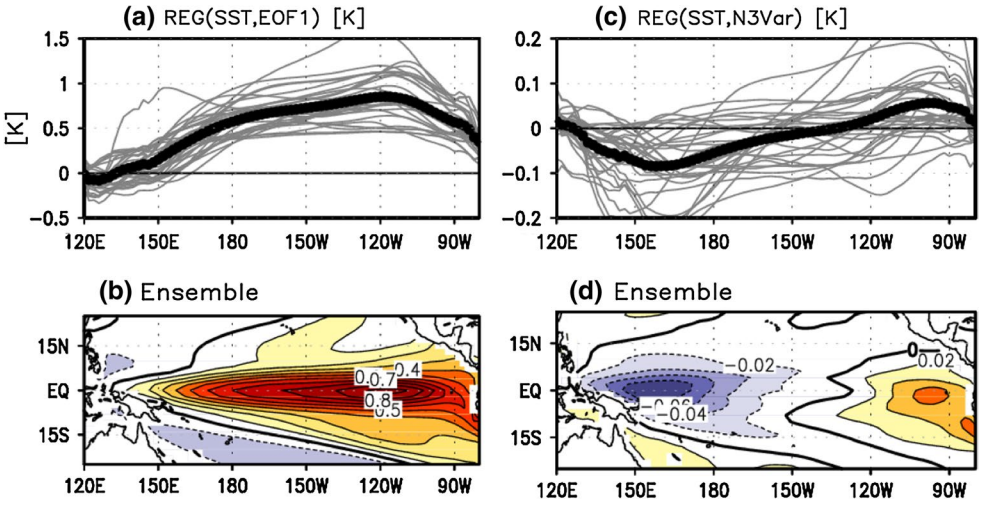

Fig. 2 **a** Regression of the equatorial-band (5°S–5°N) average SST anomaly against the PC time series of the first EOF of the tropical Pacific SST anomaly obtained from the PI experiment of CMIP5. Each line indicates the regression from each model. **b** As in (**a**) but for the tropical Pacific domain and ensemble average of all regression maps. **c**, **d** As in (**a**) and (**b**), respectively, but for the normalized N3Var index. Units are K

The computed PZM pattern (Fig. 2d) was projected to the tropical SST anomalies, resulting in a time series of the projected coefficient values. This time series represents the intensity of the PZM. Then correlation between the 7-year running average projected coefficient and the N3var index was computed. The resulting temporal correlation coefficients are presented in the last column of Table 2. Without exception, all models produced statistically significant (95 % confidence level) positive correlations, indicating that the PZM is strongly associated with changes in ENSO amplitude on a decadal-to-interdecadal time scale (Table 2).

Choi et al. (2013) referred to this dipole pattern (i.e., PZM) as 'ENSO-induced tropical Pacific decadal mode', because the nonlinear rectification due to El Nino–La Nina asymmetry can induce this pattern. During the active ENSO period (large amplitude), El Nino is dominated by eastern Pacific (EP) type, while La Nina is dominated by central Pacific (CP) type. The residual resulting from El Nino–La Nina asymmetry becomes the warm-east and cold-west pattern. On the other hand, during the inactive ENSO period (small amplitude), El Nino and La Nina are dominated by CP type and EP type, respectively, and thus the resulting residual becomes the warm-west and cold-east pattern. Therefore, the residual pattern during the active ENSO period resembles the PZM pattern in the SST, and that during the inactive ENSO period resembles the opposite pattern of PZM (Sun and Yu 2009). On the other hand, Choi et al. (2009, 2012) argued that two-way feedback between the mean climate state and ENSO is mutually reinforcing. The positive correlations in Table 2 support their argument.

To see whether PZM is realistic, we perform the same analysis using various observed SST data sets. As indicated in Sect. 2, four different data sets are utilized. Due to poor data quality prior to the 1950s, data from 1951 through the recent year (see Sect. 2) are used in this calculation. The linear trend has been removed before computation. All four data sets regularly show PZM-like patterns, although two poles (especially the negative pole over the western Pacific) are located southward compared with the models. In addition, a weak warming exists over the far-western tropical Pacific (Fig. 3). Consequently, PZM patterns associated with changes in ENSO amplitude, especially on the decadal-to-interdecadal time scale, are quite robust (Figs. 2, 3).

To obtain insights as to why the PZM is related to ENSO amplitude change, the regression patterns of other variables against N3var index are also computed. Figure 4 represents the ensemble-averaged tropical Pacific surface zonal wind stress and the precipitation patterns associated with the N3var index obtained from CMIP5 multi-model ensemble. We used the same models as in the computation of the data shown in Fig. 2. As shown in the regression map of the surface zonal wind stress (Fig. 4a), the trade wind over the central-to-eastern equatorial Pacific has been weakening. This is dynamically consistent with the weakened zonal SST gradient between the western and eastern tropical Pacific (Fig. 2d; e.g., Lindzen and Nigam 1987). The precipitation map (Fig. 4b) shows the reduced precipitation over the tropical western Pacific and the increased precipitation over the tropical central-to-eastern Pacific.

The subsurface patterns of ocean temperature associated with the ENSO index and the N3var index are also computed using the equatorial ocean temperature (5°S–5°N) from the surface to 250 m in depth. Due to the heavy load in collecting ocean subsurface data during the entire PI integration period, only one CGCM output is used (CCSM4 results). In CCSM4, the patterns of SST, zonal wind stress, and precipitation associated with the N3var index resemble the patterns of a multi-model ensemble (not shown). The subsurface temperature associated with the ENSO index is warm over the central-to-eastern Pacific and cold over the

Table 2 Linear trends of the global mean (80°S–90°N) surface air temperature (GMT) from each model and RCP scenario experiment

	Model	Linear trend of GMT		PI COR (N3Var-7 year PZM)
		RCP4.5	RCP8.5	
1	ACCESS1-0	2.23	4.76	0.45*
2	ACCESS1-3	2.15	4.66	0.47*
3	BCC-CSM1-1	1.49	3.94	0.44*
4	BNU-ESM	2.00	4.94	0.87*
5	CanESM2	2.24	4.98	0.47*
6	CCSM4	1.55	4.11	0.87*
7	CESM1-BGC	1.46	4.00	0.85*
8	CNRM-CM5	2.02	4.12	0.71*
9	CSIRO-Mk3.6	2.50	4.84	0.62*
10	FGOALS-G2	1.20	3.49	0.72*
11	GFDL-CM3	2.60	5.25	0.75*
12	GFDL-ESM2G	0.91	3.31	0.59*
13	GFDL-ESM2 M	1.05	3.11	0.81*
14	GISS-E2-H	1.39	3.24	0.80*
15	GISS-E2-H-CC	1.20	–	0.73*
16	GISS-E2-R	1.02	2.77	0.66*
17	GISS-E2-R-CC	1.00	–	0.56*
18	HadGEM2-CC	2.42	5.39	0.53*
19	HadGEM2-ES	2.61	5.25	0.44*
20	INMCM4	1.37	3.18	0.41*
21	IPSL-CM5A-LR	2.24	5.27	0.32*
22	IPSL-CM5A-MR	2.22	5.18	0.38*
23	IPSL-CM5B-LR	1.74	3.98	0.66*
24	MIROC5	1.70	3.83	0.74*
25	MIROC-ESM	2.56	5.47	0.26*
26	MIROC-ESM-CHEM	2.63	5.70	0.40*
27	MPI-ESM-LR	1.50	4.10	0.40*
28	MPI-ESM-MR	1.66	4.14	0.32*
29	MRI-CGCM3	1.77	3.95	0.41*
30	NorESM1-M	1.66	3.72	0.52*
31	NorESM1-ME	1.72	3.93	0.76*
	Ensemble mean	1.80	4.30	

Units are in K 100 year^{-1} . The last column represents the temporal correlation between the N3Var index and the seven-year moving averaged-projected coefficients of the PZM pattern in the PI simulation

* Statistically significant at 95 % confidence level

western Pacific. Most notably, the maximum positive and negative loadings are found in the eastern pacific around a 50 m depth, and the western Pacific around a 150 m depth, respectively (Fig. 5a). This pattern resembles the pattern during the mature state of El Nino, which is associated with a weakened trade wind. The subsurface pattern associated with the N3var index also shows a warm-east and cold-west pattern (Fig. 5b). However, unlike the ENSO pattern, the maximum negative loading is located only about 40 m deeper than the maximum positive loading, and the amplitudes of the two poles are smaller than the ENSO pattern. This pattern is quite similar to the ENSO-induced tropical Pacific decadal variability pattern of Choi et al. (2013, see their Fig. 2).

Previously, we identified the SST pattern associated with ENSO amplitude change, but the merits of this approach are debatable because of unclear causality. In other words, the regression pattern associated with ENSO amplitude is either caused by the change in the ENSO itself, such as a nonlinear process (Timmermann et al. 2003), or is causing change in ENSO amplitude (Fedorov and Philander 2000; An and Wang 2000). Interactive feedback between the mean state and ENSO is also a possible mechanism (Choi et al. 2009, 2012). Nevertheless, there are dynamical reasons as to how the patterns associated with the N3var index, i.e., PZM could influence ENSO amplitude. As shown in Fig. 4b, the positive precipitation over the central-to-eastern Pacific indicates a low-level convergence anomaly, indicating intensified low-level background convergence. When a perturbed low-level convergence occurs over this region due to the positive SST anomaly, it is intensified by the low-level background convergence through convergence feedback, namely that the perturbed convective heating generates low-level convergence, which carries more moisture into the initial convergence region (Zebiak and Cane 1987; Kang and Kug 2002). This indicates an intensified air-sea coupling. Strong air–sea coupling obviously leads to a strong El Nino. Choi et al. (2009) performed a stability analysis of the linearized intermediate tropical Pacific atmosphere–ocean model that had been particularly designed to simulate the ENSO phenomenon, in which the altered background states, i.e., zonal dipole SST pattern, which resembles PZM SST pattern, are prescribed. In the sensitivity experiment, they found that the growth rate of the ENSO mode increased under the zonal-dipole SST pattern, mainly due to the intensified atmospheric heating associated with the zonal dipole SST pattern. The intensification of ENSO in their experiment is also related to the eastward migration of the action center due to the warming of the cold tongue. Since the action center associated with El Nino moves to the east, the delayed negative feedback by the upwelling oceanic Rossby wave is further delayed and the El Nino has more time to grow (Wang and An 2001, 2002). This results in an increase in ENSO amplitude. On the whole, the PZM and the associated atmospheric change provide a favorable condition for intensification of the ENSO.

4 Future change in ENSO amplitude

In the previous section, we showed the tropical Pacific climate pattern associated with change in ENSO amplitude

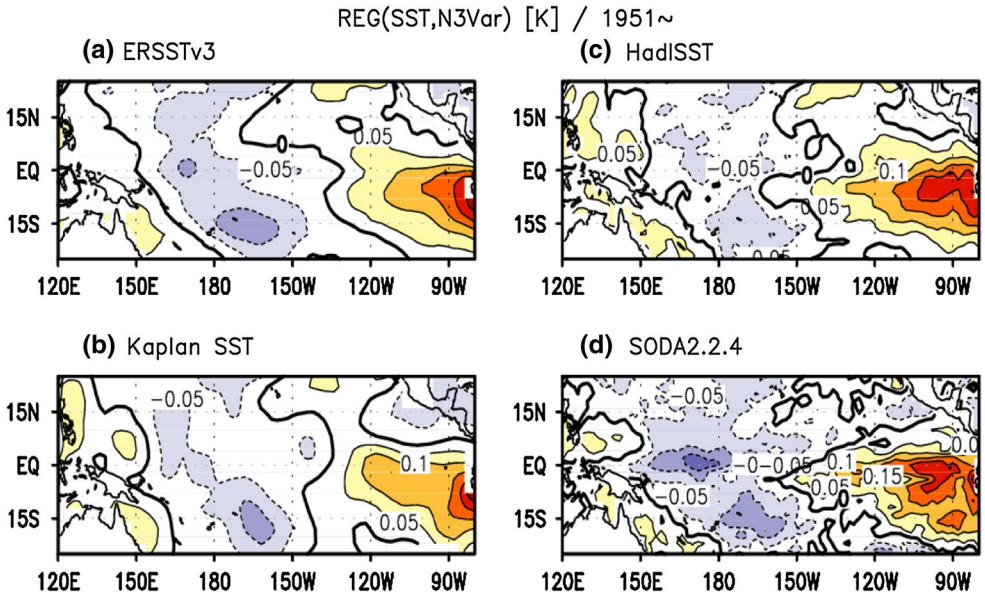

Fig. 3 Regression map of tropical Pacific SST anomalies against the N3var index obtained from **a** ERSSTv3 (January 1951–November 2012), **b** Kaplan SST (January 1951–November 2012), **c** HadISST (January 1951–September 2012), and **d** SODA2.2.4 SST (January 1951–December 2008). Units are K. The linear trend has been removed. Contour intervals are 0.05

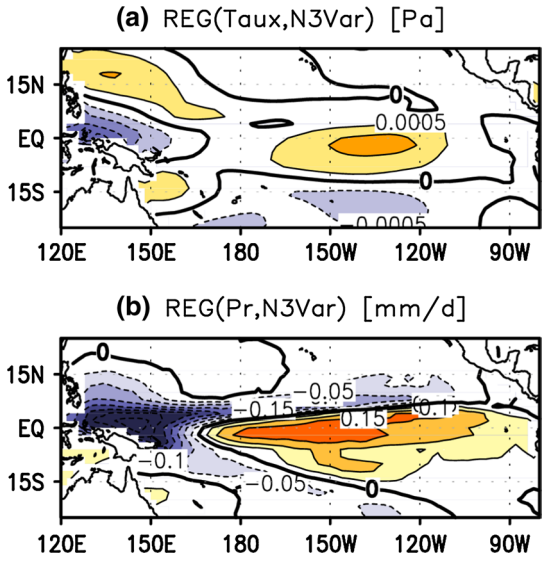

Fig. 4 Ensemble regression of **a** surface zonal wind stress and **b** precipitation anomalies against the normalized N3var index obtained from the PI experiment of CMIP5. Units are Pa for (**a**) and mm day^{-1} for (**b**)

(identified as the PZM). In this section, we address why the future change in ENSO amplitude is uncertain. First, we check the validity of the PZM in two scenarios: RCP4.5 and RCP8.5. To compute the SST pattern associated with change in ENSO amplitude, the same computation methods used in the previous section are applied to RCP4.5 and RCP8.5 data sets. Since both RCP4.5 and RCP8.5 have significant linear trends, the data are de-trended. The PZM is clearly observed in both RCP4.5 and RCP8.5, although each model's results show scattered features (Fig. 6). In other words, PI, twentieth century observations, RCP4.5, and RCP8.5 commonly represent the PZM as the pattern associated with change in ENSO amplitude.

Next, we compute the linear SST trend using the raw data in two scenario experiments: RCP4.5 and RCP8.5. The linear trend of the global mean surface air temperature (GMT) of each model is listed in Table 2. In general, the tropical SST trend is smaller than the global mean surface air temperature trend. In both experiments, the entire Pacific shows a positive SST trend with the exception of one CGCM. This strong trend is observed over the tropical eastern Pacific, and thus the patterns of both experiments are quite similar (Fig. 7). The trend in RCP8.5 is greater than that in RCP4.5. Only one CGCM (FGOALS-G2) simulated the cooling trend over the equatorial Pacific in both scenario experiments. Overall, the linear trend pattern of the SST has a basin-wide warming pattern, but is different from the PZM. As shown in the previous section, the PZM is the most coherent pattern with change in ENSO amplitude; however, the linear trend pattern is not similar to the PZM. For example, the pattern correlations between the PZM (Fig. 6b, d) and the linear trend pattern (Fig. 7b, d) are less than 0.20 for both RCP4.5 and RCP8.5.

The linear trends of the surface zonal wind stress and precipitation are computed using RCP4.5 and RCP8.5. As shown in Fig. 8, the trade wind over the northern western-to-central Pacific is weakened, and that over the southern eastern Pacific is intensified. The precipitation over the equatorial western Pacific is increased more than that over the equatorial eastern Pacific. The two patterns are almost the opposite of those associated with the PZM (i.e., the drying over the western Pacific and the wetting over the eastern Pacific; Fig. 4). It should be noted that the significance

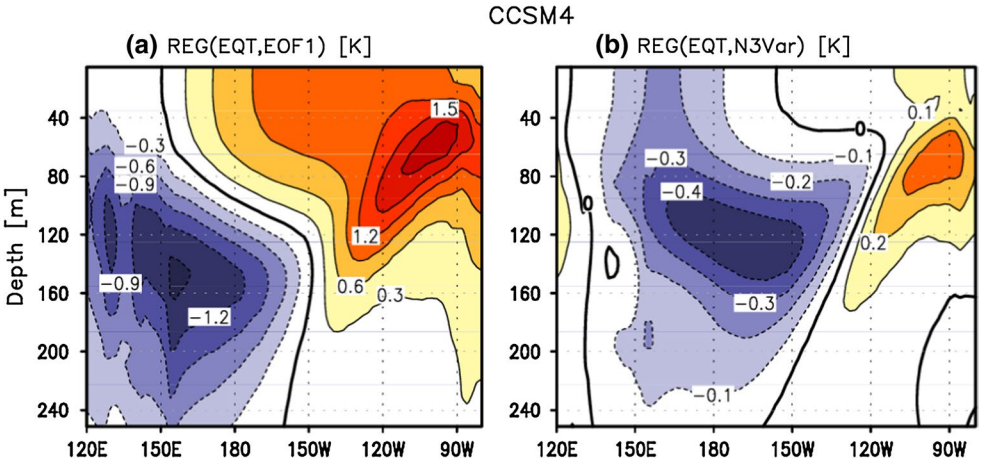

Fig. 5 **a**, **b** As in Fig. 1b, d, respectively, but for the subsurface ocean temperature along the equatorial Pacific band (5°S–5°N) from CCSM4 of CMIP5

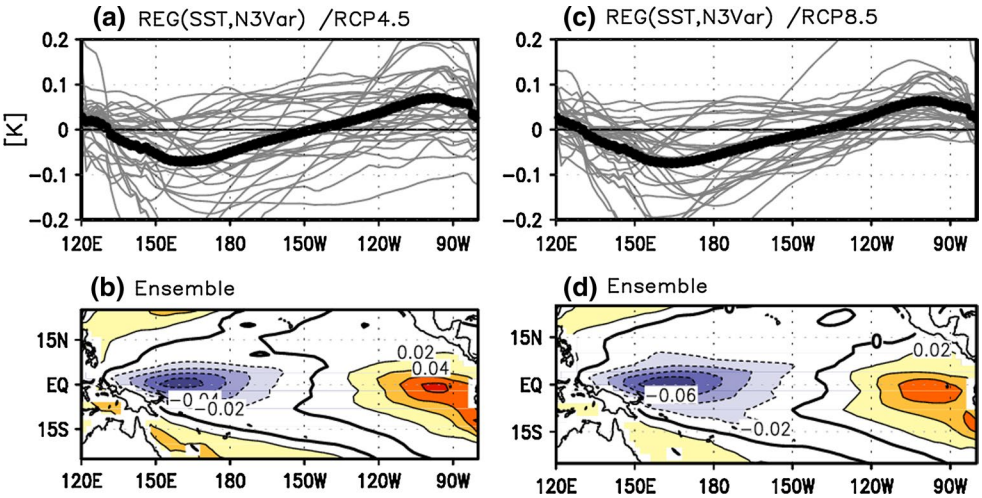

Fig. 6 **a** Regression of the de-trended equatorial-band (5°S–5°N) average SST anomaly against the PC time series of the normalized de-trended N3Var index obtained from the RCP4.5. Each *line* indicates the regression from each model. **b** As in (**a**) but for the tropical Pacific domain and ensemble average of all regression maps. **c**, **d** As in (**a**) and (**b**), respectively, but for the RCP8.5. Units are K

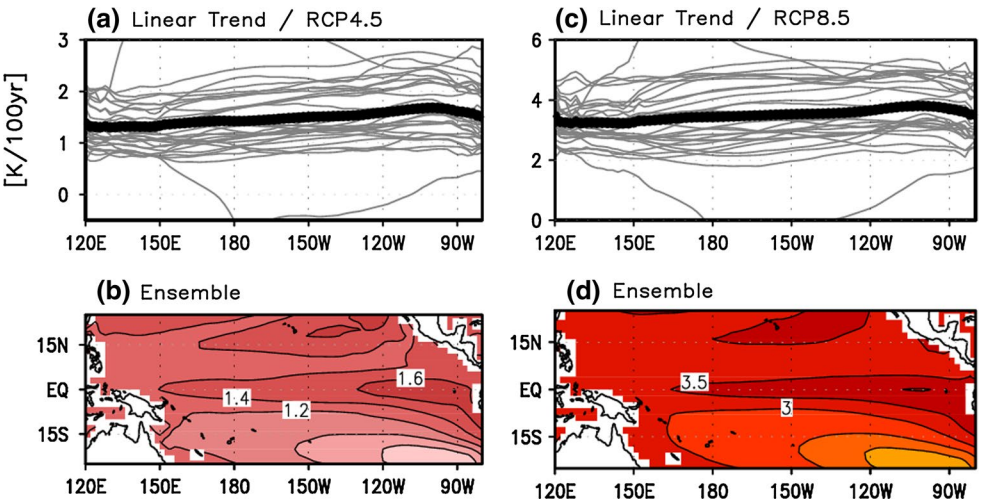

Fig. 7 **a** Linear trend of the equatorial-band average SST anomaly from the RCP4.5 scenario experiment. Each *line* indicates the linear trend obtained from each model. **b** Ensemble mean of the linear trend of the tropical Pacific SST from the RCP4.5 scenario experiment. **c** As in (**a**) but for RCP8.5. **d** As in (**b**) but for RCP8.5. Units are K 100 years^{-1}

of these ensemble patterns is rather weak because of considerable scattering among the models. Nevertheless, it is expected that the pattern of Fig. 8 could lead to suppressed or static ENSO activity through the reduction of the air–sea coupling with the same reason as PZM could intensify ENSO activity but in an opposite way. Therefore, the linear

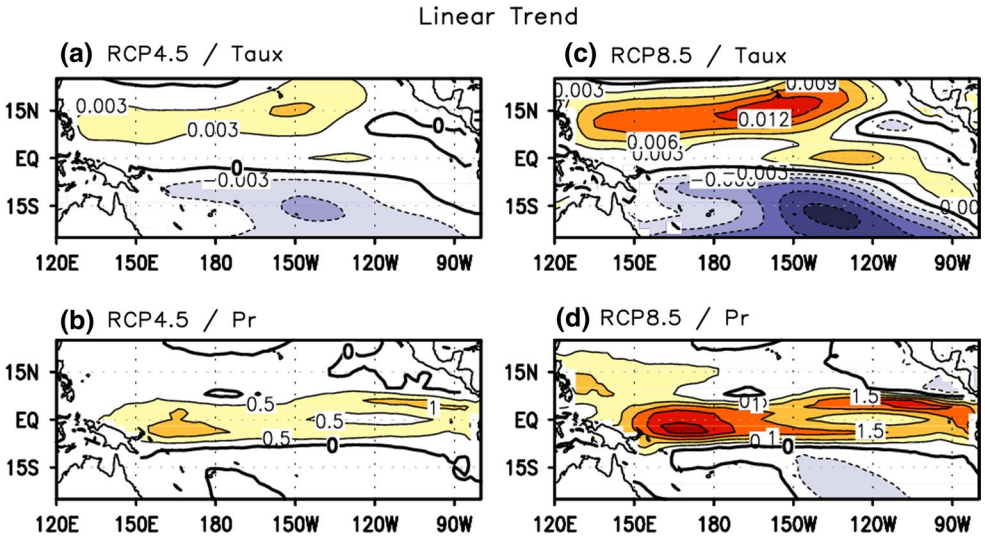

Fig. 8 The linear trend of the zonal wind stress anomaly from **a** RCP4.5 and **b** RCP8.5 scenario experiments. **c**, **d** As in (**a**) and (**b**) but for precipitation. Units are Pa 100 years^{-1} and mm day^{-1} 100 years^{-1}

trend pattern, i.e., the global warming signal cannot significantly influence ENSO amplitude.

5 Intermediate coupled model (ICM) experiment

To further confirm the impacts of the linear trend pattern (i.e., basin-wide warming with an emphasis over the eastern tropical Pacific) and the PZM pattern on ENSO amplitude, we performed two types of numerical model simulations: a fixed SST anomaly forcing experiment (EXP1) and the prescribed mean SST experiment (EXP2) using an intermediate coupled ocean–atmosphere model[1] (see Sect. 2 for model details). The main difference between EXP1 and EXP2 is that EXP1 modifies all physical values linked to a fixed SST perturbation so examining the general effect of two different SST pattern but EXP2 modifies only the atmospheric heating.

For EXP1, we imposed the SST forcing associated with the linear trend (or PZM) pattern to the SST equation of the model as like an anomalous heat flux:

$$\frac{dT'}{dt} = -\alpha T' - (\bar{u}+u')\frac{\partial T'}{\partial x} - u'\frac{\partial \bar{T}}{\partial x} - (\bar{v}+v')\frac{\partial T'}{\partial y} - v'\frac{\partial \bar{T}}{\partial y} - M(\bar{w})\frac{\partial T'}{\partial z} - \{M(\bar{w}+w') - M(\bar{w})\}\frac{\partial \bar{T}}{\partial z} + \gamma Q, \quad (1)$$

where γ is a control factor for the intensity of forcing with the inverse of time unit, and Q is the linear trend or PZM SST patterns. Since Q acts as a steady state forcing, the winds and the horizontal and vertical currents will adjust to a given SST forcing after a few time steps of integration. In this manner, the Q pattern influences the model's behaviors. Similar idea was used in a transient run for simulating the ENSO variability of the late interglacial period (Clement et al. 2000). Since the maximum values of each pattern are different, the two SST forcing (i.e., the linear trend and PZM patterns) are divided by their own average value over the Nino-3 region. Thus, the magnitudes of SST forcing over Nino-3 region become 1 (°C/time) in both the linear trend and PZM experiments. Here, we perform 400-year integration for each run, and the last 200 years of outputs are utilized. Since our focus is the ENSO amplitude, the standard deviation is computed from each run. To check the reliability of the model's sensitivity, we repeat the experiments with a slightly altered coupling parameter (±2 % of control value). As shown in Fig. 9, when the PZM pattern is applied, the ENSO intensity significantly increases as the intensity of forcing increases (e.g., 1/25-year run has stronger forcing than the 1/100-year run). The ENSO intensity slightly decreases when the linear trend pattern is applied. The perturbed coupling parameter still provides a consistent result.

In EXP2, in order to examine the response of the atmosphere to SST change, we change the background mean SST states only in the atmosphere model. The reason to perform

[1] Conceptually, ICM system used in EXP1 can be written as $\frac{d\vec{X}}{dt} = \boldsymbol{f}(\vec{X}_0, \vec{X}) + \gamma\vec{Q}$, where **f** is a differentiable vector field, $\vec{X}$ is a state vector of perturbation for atmospheric and oceanic variables, and $\vec{X}_0$ is its mean vector. Since $\vec{X}_0$ is a constant vector, $\vec{Q}$ continuously modifies $\vec{X}$ as to satisfy $\frac{d\vec{X}}{dt} = 0$. Therefore, ICM system becomes $\frac{d\vec{X}}{dt} \approx \boldsymbol{f}(\vec{X}_0, \vec{X} + \vec{X}_Q)$, especially when nonlinear terms in ICM are relatively small compared to the linear terms, where $\vec{X}_Q$ is a constant vector for $\boldsymbol{f}(\vec{X}_0, \vec{X}_Q) = \gamma\vec{Q}$. On the other hand, ICM system for EXP2 can be $\frac{d\vec{X}}{dt} = \boldsymbol{f}(\vec{X}_0, \Delta\vec{X}_0 + \vec{X})$, where $\Delta\vec{X}_0$ is a vector to represent the linear trend SST pattern or PZM SST pattern. Therefore, in EXP1, a Jacobian matrix for the linear stability of the original ICM system may not be changed but the equilibrium states (a.k.a. fixed point) are changed, while in EXP2, the Jacobian matrix is changed.

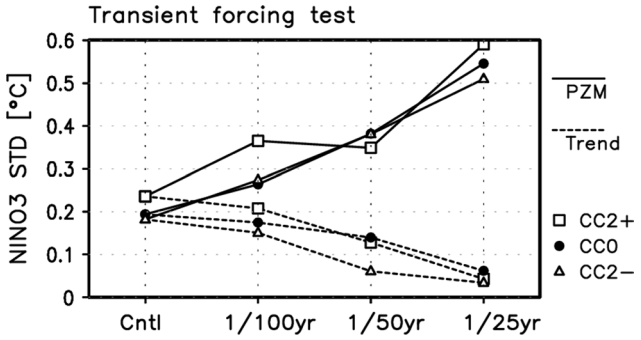

Fig. 9 Standard deviation of the Nino-3 index with respect to the relaxation time scale toward the forced surface-heating rate obtained from the intermediate model experiment. *Solid* and *dashed lines* indicate the model sensitivity to the SST pattern associated with the PZM and the linear SST trend pattern, respectively. The simulations with different coupling strength are marked by *rectangles* (2 % increase), *closed circles* (control), and *triangles* (2 % decrease)

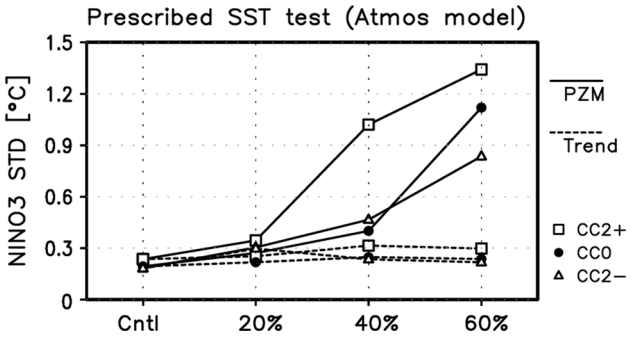

Fig. 10 Standard deviation of the Nino-3 index with respect to the prescribed mean SST in the atmospheric model obtained from the intermediate model experiment. *Solid* and *dashed lines* indicate the model sensitivity to the SST pattern associated with the PZM and the linear SST trend pattern, respectively. The simulations with different coupling strength are marked by *rectangles* (2 % increase), *closed circles* (control), and *triangles* (2 % decrease)

this experiment is that the increasing water vapor content in the atmosphere and so latent heat is considered as the first order response of the tropical atmosphere to the global warming. Therefore, it is worthy to be checked as to how much this specific process influences ENSO variability. In this ICM, the latent heating, i.e. convective heating in the atmosphere, (Q0) is parameterized based on the mean SST (T_c) and SST anomaly (SSTA) as follows:

$$Q0 = \alpha \times SSTA \times \exp[(T_c - 30^{\circ}C)/17.0], \quad (2)$$

where α is a conversion parameter for latent heat. Therefore, a warmer or cooler mean SST modifies the sensitivity of the convective heating to the changes in SSTA. Similar to the previous experiments, both the linear trend and PZM SST patterns are divided by each average value over the Nino3 region. Then, T_c in the above equation is replaced by T_c*, where $T_c^* = T_c + \beta\Delta$. The Δ is the SST pattern of the linear trend or the PZM, and β is set to 0.2, 0.4, and 0.6. In other words, 20, 40, and 60 % of the linear trend and PZM SST patterns is added to the original mean SST states of ICM. Note that we only tuned atmospheric heating parameterization by modifying the mean SST state. The background state in the ocean model is the same as the control experiment. Therefore, this experiment measures the sensitivity on how much each SST pattern influences ENSO variability through modifying the atmospheric convective heating (physically, the surface evaporation rate against to SST change). For example, the linear trend SST pattern will increase the sensitivity over the whole Pacific because of the basin-wide warming, while the PZM SST pattern will increase it over the tropical eastern Pacific but decrease it over the tropical western Pacific. As a result, the PZM SST pattern would promote the sensitivity of convective heating only over the eastern Pacific, while the linear trend SST pattern, i.e., the basin-wide warming, would enhance the whole Pacific basin. A possible consequence associated with change in the convective heating center has been mentioned in the Sect. 3.

Here, we performed 400-year integration for each run, and the last 200 years are used to calculate the ENSO amplitude. As shown in Fig. 10, the ENSO amplitude significantly increases as the intensity of forcing increases when the PZM pattern is prescribed. On the other hand, the change in ENSO intensity is insignificant when the linear trend pattern is prescribed. Note that the sensitivity to the coupling strength was prominent in PZM case but not stood out in the linear trend case.

In order to figure out the main process for the intensification of ENSO in EXP2, we computed SST tendency terms of each experiment (see Eq. 1) and then draw the lagged regression map of SSTA and SST tendency terms against to Nino-3 SSTA [for the control case, see An et al. (1999)]. Basically such lagged regression map indicates the evolution of SST tendencies in a canonical ENSO cycle. Figure 11 shows the difference between two results. Figure 11a represents the evolution of SSTA difference between two experiments along the equator associated with ENSO. This SSTA difference is mainly attributed to the positive SST tendency due to the zonal (Fig. 11b), meridional (Fig. 11c) and vertical (especially due to anomalous upwelling; Fig. 11e) advections. The vertical advection by mean upwelling (Fig. 11d) increases the eastern Pacific SST but decreases the central Pacific SST.

Since the oceanic mean states is not perturbed, the main cause for such intensification is due to the air–sea coupling. This is because all three positive SST tendency terms are linearly proportional to the air–sea coupling strength. Here we also computed the air–sea coupling strength, which is

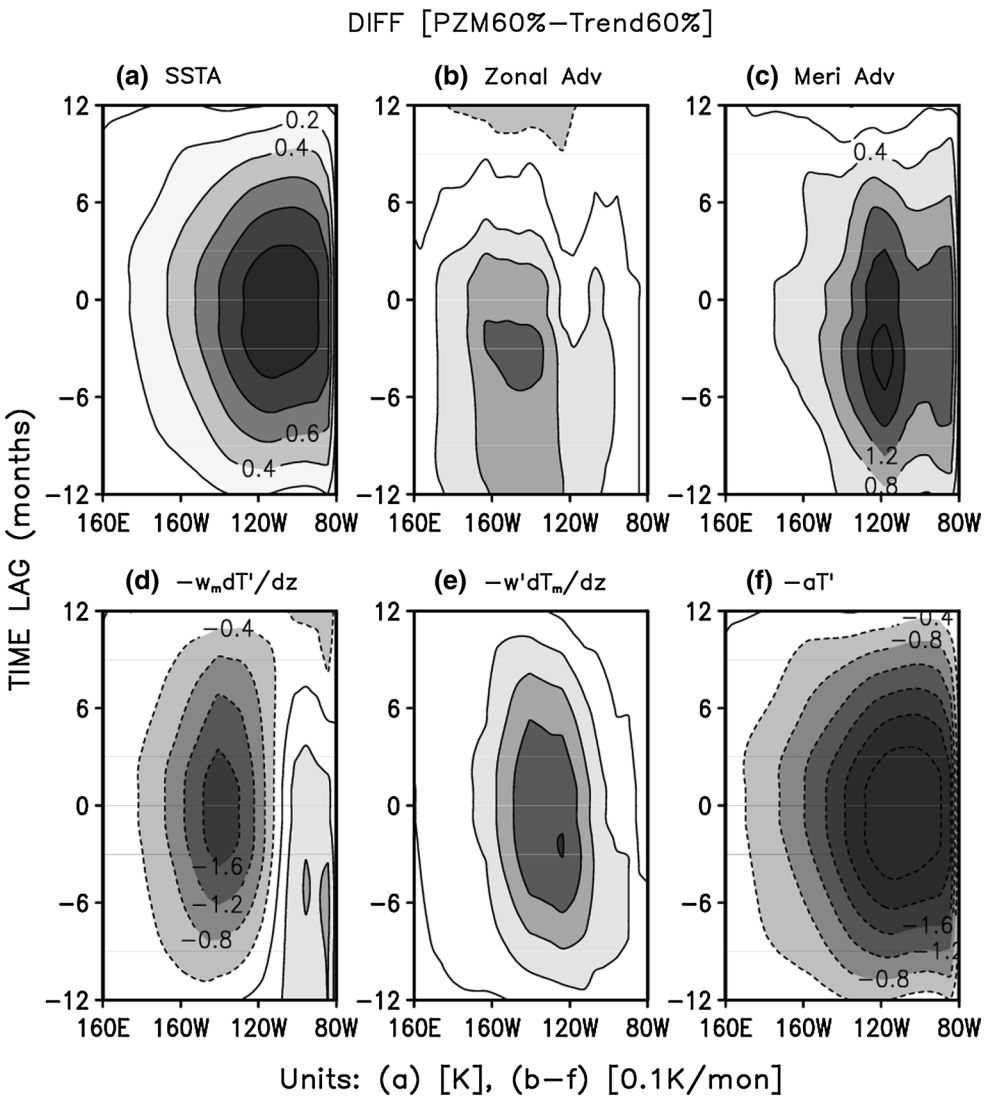

Fig. 11 Regression maps of SST anomaly (**a**), zonal advection (**b**), meridional advection (**c**), vertical advection by mean upwelling (**d**) and anomalous upwelling (**e**), and the thermodynamical damping (**f**), against Nino-3 SST anomaly along the equator (5°S–5°N) obtained from EXP2. Units are K (**a**), and K month^{-1} for all others

measured by the regression of the equatorial surface zonal wind stress against Nino-3 index. Zonal mean values of the regression coefficients are 6.9 (10^{-3} Pa K^{-1}) for PZM-pattern experiment and 6.6 (10^{-3} Pa K^{-1}) for the trend-pattern experiment. Thus, the coupling strength for PZM-pattern experiment is larger than that for the trend-pattern experiment. More importantly, as shown in Fig. 12, the difference in the longitudinal location of the maximum wind stress between two experiments is about 25°, which is similar to the observed decadal change between pre-1980s and post-1980s (An and Wang 2000). During these two decades, a significant change in ENSO amplitude was recorded (An and Wang 2000). As mentioned in Sect. 3, on the dynamical consequence between ENSO amplitude and the zonal location of action center, further eastward migration of action center due to PZM pattern leads to the intensification of ENSO.

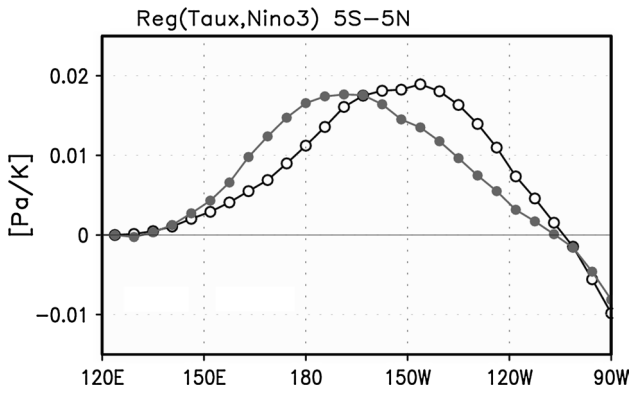

Fig. 12 Regression curves of the equatorial zonal wind stress anomaly (5°S–5°N) against Nino-3 SST anomaly along the equator (5°S–5°N). Open and close dots indicate the results from EXP2 when the PZM and linear trend patterns are employed with 60 % rate, respectively

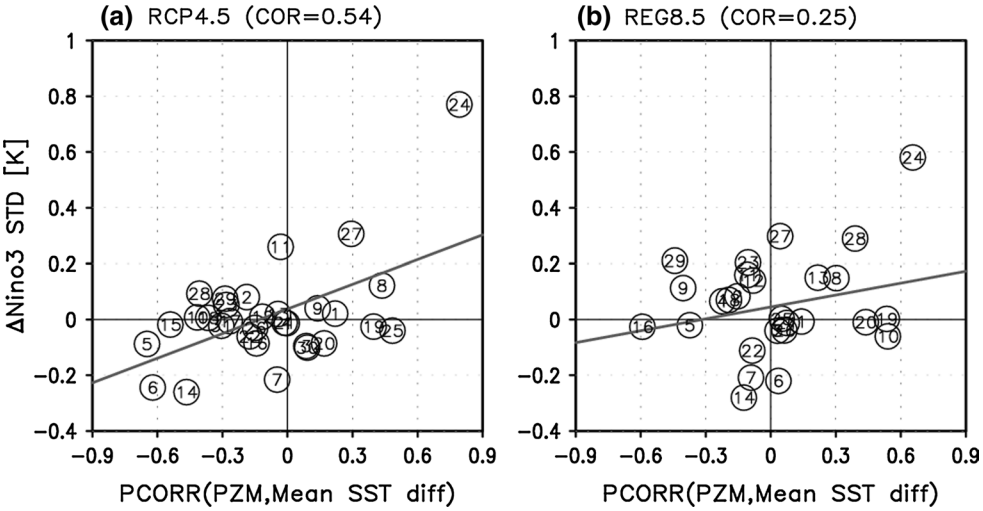

Fig. 13 **a** Scatter plot of a pattern correlation between mean SST change (RCP4.5 minus PI) and PZM verse difference in Nino-3 standard deviation (RCP4.5 − PI). **b** As in (**a**) but for RCP8.5. *Number* in the *circle* indicates model number shown in Table 1 of main text

In summary, we found that zonal dipole-like mean SST changes (i.e., PZM pattern) could efficiently alter ENSO intensity through changes in atmosphere sensitivity, as mentioned in Sect. 3, while the basin-wide SST warming (i.e., linear trend pattern) could not significantly influence ENSO amplitude. On the whole, the intermediate model experiment supports the results of the previous analysis.

6 Summary and discussion

In this study, we initially focused on the decadal modulation of ENSO amplitude through the internal process. In most of the CGCMs, the decadal modulation range of ENSO amplitude is larger than the differences in ENSO amplitudes between the PI and RCP experiments. Based on the regression method, we found that the most coherent SST pattern to the change of ENSO amplitude is the zonal dipole pattern (PZM) in the PI simulation. It was also found that this PZM is consistently observed in the four observation data sets. The PZM leads to the reduction of the zonal gradient of the mean SST, and the consequential weakening of trade winds. The associated precipitation over the central-to-eastern Pacific increases, while that over the western Pacific decreases, and thus resulting in the eastward shift of ENSO-induced convection center. In addition, the subsurface temperature anomalies associated with the PZM also show a zonal dipole structure. The PZM patterns are also observed in the RCP experiments with CMIP5; this indicates that the PZM is the robust mode.

We next examined the impact of climate change trend. The linear trend of the SST obtained from RCP experiments shows a basin-wide warming relatively weighted over the tropical eastern Pacific different from that of the PZM. The corresponding surface zonal wind stress and precipitation patterns show very different features compared with the PZM. The linear trend pattern of zonal wind stress shows north–south asymmetry. In addition, the precipitation increases at the equator in the RCP experiments, while the western equatorial Pacific is wetter than the eastern equatorial Pacific. Consequently, the atmospheric changes associated with the linear trend show very different features from those of the counterparts of the PZM.

To investigate the relationship between mean SST change and ENSO variability change in RCP experiment, first we compute a pattern correlation between difference of mean SST (RCP minus PI) and PZM pattern, and then draw a scatter plot of the pattern correlation verse difference of the standard deviation of Nino-3 index (RCP minus PI) in Fig. 13. The pattern correlation indicates how far the mean SST pattern from RCP resembles PZM pattern compared to that from PI. The result shows a strong positive correlation between two quantities. It indicates that as the mean tropical Pacific SST pattern in RCP experiment (RCP4.5 and 8.5) becomes more similar to PZM pattern compared to the PI experiment, ENSO variability in RCP also increases more, inferring that PZM pattern could cause the intensification of ENSO variability. Note that MIROC5 (Model 24) recorded the largest pattern correlations as well as the largest change in the standard deviation of Nino-3 index.

In order to identify the dynamical process on the intensification of ENSO, we further analyzed data, and performed ICM experiments. First, the linear trend and PZM patterns are forced to the SST tendency equation. Second, both SST patterns are prescribed in the atmospheric latent heating term. Both experiments produce consistent results: the PZM pattern leads to the intensification of the ENSO, but the linear trend pattern does not. The PZM pattern (i.e., warm-east and cold-west) and the associated enhancement of precipitation over the central-to-eastern Pacific increase the air–sea coupling, and it has the ENSO-induced zonal wind patch be shifted to the east, which increases ENSO

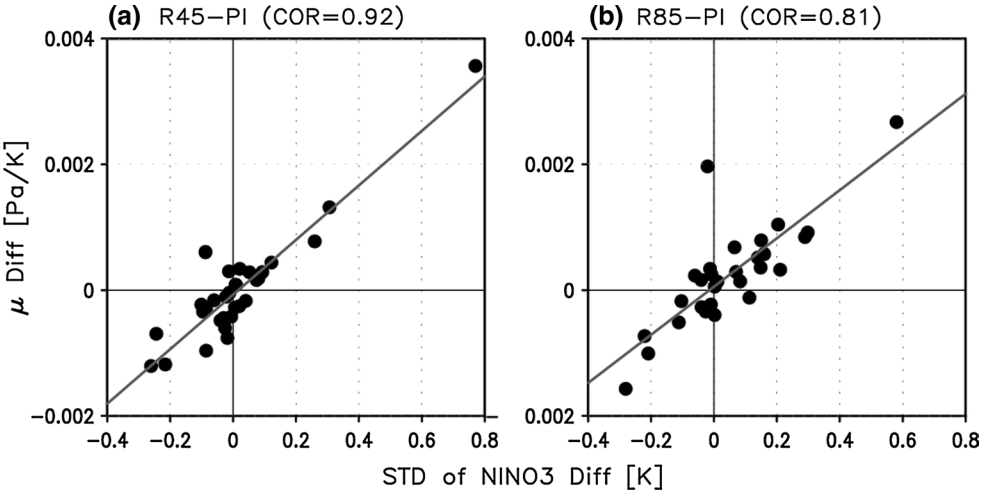

Fig. 14 Multi-model relationship between changes in ENSO amplitude and air–sea coupling strength (μ). **a**, **b** The difference between the control experiment and that from RCP4.5 and RCP8.5, respectively

amplitude by delaying the negative feedback. In addition, the reduction of the trade wind weakens the anomalous thermal advection by the mean meridional overturning circulation in the tropical Pacific due to the weakening of the pole-ward Ekman current, which weakens the damping of the ENSO (An et al. 2004). As a result, ENSO amplitude increases under PZM-like mean states. On the other hand, when the linear trend patterns are applied, the ENSO intensity slightly decreases or is not significantly changed as the forcing increases. The increased precipitation over the western Pacific promotes the shift of the action center of ENSO to the west; this causes a fast returning of the upwelling Rossby wave (so-called 'delayed negative feedback') so that the ENSO quickly damps. In addition, the intensification of the trade wind over the eastern Pacific could lead to the strengthening of the poleward Ekman current, which causes strong damping of ENSO by thermal advection. Lastly, the intermediate model simulations verify that the linear trend pattern of the SST slightly suppresses ENSO amplitude, while the PZM intensifies ENSO.

The question remains as to what dynamical processes control ENSO intensity in the future climate. In order to answer the question, we examined the sensitivity of the atmosphere to the SST anomaly in each model. We computed the air–sea coupling strength (μ) in BJ index (Jin et al. 2006; Kim and Jin 2011) as defined by the linear regression coefficient between the zonal mean (120°E–80°W, τ'), zonal wind stress anomaly, and the Nino-3 SST anomaly ($\tau' = \mu T'$). Figure 14 represents the multi-model relationship between changes in the Nino-3 standard deviation and μ. The two parameters are highly positively correlated in both RCP4.5 (0.92) and RCP8.5 (0.81) runs, indicating larger air–sea coupling results in the larger change in ENSO amplitude. The air–sea coupling strength is an important factor in the modification of ENSO amplitude in the future climate. However, more comprehensive analysis is needed in order to understand the role of ocean structure on ENSO intensity.

Acknowledgments This work was supported by the National Research Foundation of Korea Grant funded by the Korean Government (MEST) (NRF-2009-C1AAA001-2009-0093042 and 2011-001508) and by NSF grant AGS-1233542. We acknowledge the World Climate Research Programme's Working Group on Coupled Modeling, which is responsible for CMIP, and we thank the climate modeling groups (listed in Table 1 of this paper) for producing and making available their model output.

References

An S-I (2009) A review of interdecadal changes in the nonlinearity of the El Nino-Southern Oscillation. Theor Appl Climatol 97:29–40

An S-I, Jin F-F (2000) An eigen analysis of the interdecadal changes in the structure and frequency of ENSO mode. Geophys Res Lett 27:1573–1576

An S-I, Jin F-F (2004) Nonlinearity and symmetry of ENSO. J Clim 17:2399–2412

An S-I, Wang B (2000) Interdecadal change of the structure of the ENSO mode and it impact on the ENSO frequency. J Clim 13:2044–2055

An S-I, Jin F-F, Kang I-S (1999) The role of zonal advection feedback in phase transition and growth of ENSO in the Cane-Zebiak model. J Meteor Soc Japan 77:1151–1160

An S-I et al (2004) Modeling evidence for enhanced El Nino-Southern Oscillation amplitude during the Last Glacial Maximum. Paleoceanography 19:PA4009

An S-I, Ham Y-G, Kug J-S, Jin F-F, Kang I-S (2005) El Nino–La Nina asymmetry in the coupled model Intercomparison project simulations. J Clim 18:2617–2627

An S-I, Kug J-S, Ham Y-G, Kang I-S (2008) Successive modulation of ENSO to the future greenhouse warming. J Clim 21:3–21

Borlace S, Cai W, Santoso A (2013) Multidecadal ENSO amplitude variability in a 1000-yr simulation of a coupled global climate model: implications for observed ENSO variability. J Clim 26:9399–9407

Carton JA, Giese BS (2008) A reanalysis of ocean climate using simple ocean data assimilation (SODA). Mon Weather Rev 136:2999–3017

Choi J, An S-I, Dewitte B, Hsieh W-W (2009) Interactive feedback between the tropical Pacific decadal oscillation and ENSO in a coupled general circulation model. J Clim 22:6597–6611

Choi J, An S-I, Yeh S-W (2012) Decadal amplitude modulation of two types of ENSO and its relationship with the mean state. Clim Dyn 38:2631–2644

Choi J, An S-I, Yeh S-W, Yu J-Y (2013) ENSO-like and ENSO-induced tropical Pacific decadal variability in CGCMs. J Clim 26:1485–1501

Christensen JH et al (2013) Climate phenomena and their relevance for future regional climate change. In: Stocker TF et al (eds) Climate change 2013: the physical science basis. Contribution of Working Group I to the Fifth Assessment Report of the Intergovernmental Panel on Climate Change. Cambridge University Press, Cambridge, UK and New York, NY, USA

Clement AC, Seager R, Cane MA (2000) Suppression of El Nino during the mid-Holocene changes in the Earth's orbit. Paleoceanography 15:731–737

Collins M et al (2010) The impact of global warming on the tropical Pacific Ocean and El Nino. Nat Geosci 3:391–397

Fedorov AV, Philander SGH (2000) Is El Nino changing? Science 288:1997–2002

Guilyardi E, Bellenger H, Collins M, Ferrett S, Cai W, Wittenberg A (2012) A first look at ENSO in CMIP5. CLIVAR Exchanges 58:29–32

Jin F-F (1997) An equatorial ocean recharge paradigm for ENSO. Part I: conceptual model. J Atmos Sci 54:811–829

Jin F-F, Kim S-T, Bejarano L (2006) A coupled-stability index of ENSO. Geophys Res Lett 33:L23708. doi:10.1029/2006GL027221

Kang I-S, Kug J-S (2002) El Nino and La Nina sea surface temperature anomalies: asymmetry characteristics associated with their wind stress anomalies. J Geophys Res 107:4372. doi:10.1029/2001JD000393

Kaplan A et al (1998) Analyses of global sea surface temperature 1856–1991. J Geophys Res 103:18567–18589

Kim B-M, An S-I (2011) Understanding ENSO regime behavior upon an increase in the warm-pool temperature using a simple ENSO model. J Clim 24:1438–1450

Kim S-T, Jin F-F (2011) An ENSO stability analysis. Part II: results from the twentieth and twenty-first century simulations of the CMIP3 models. Clim Dyn 36:1609–1627

Kim S-T, Yu J-Y (2012) The two types of ENSO in CMIP5 models. Geophys Res Lett 39:L11704. doi:10.1029/2012GL052006

Lindzen RS, Nigam S (1987) On the role of sea surface temperature gradients in forcing low-level winds and convergence in the tropics. J Atmos Sci 44:2418–2436

Meehl GA et al (2007) Global climate projections. In: Solomon S, Qin D, Manning M, Chen Z, Marquis M, Averyt KB, Tignor M, Miller HL (eds) Climate change 2007: the physical science basis. Contribution of Working Group I to the Fourth Assessment Report of the Intergovernmental Panel on Climate Change. Cambridge University Press, Cambridge, UK and New York, NY, USA

Neelin JD et al (1998) ENSO theory. J Geophys Res 103:14261–14290. doi:10.1029/97JC03424

Rayner NA et al (2003) Global analyses of sea surface temperature, sea ice, and night marine air temperature since the late nineteenth century. J Geophys Res 108:4407. doi:10.1029/2002JD002670

Smith TM, Reynolds RW (2004) Improved extended reconstruction of SST (1854–1997). J Clim 17:2466–2477

Stevenson SL (2012) Significant changes to ENSO strength and impacts in the twenty-first century: results from CMIP5. Geophys Res Lett 39. doi:10.1029/2012GL052759

Stevenson SL, Fox-Kemper B, Jochum M, Neale R, Deser C, Meehl G (2012) Will there be a significant change to El Nino in the twenty-first century? J Clim 25:2129–2145

Sun F, Yu J-Y (2009) A 10–15-year modulation cycle of ENSO intensity. J Clim 22:1718–1735

Taylor KE, Stouffer RJ, Meehl GA (2012) An overview of CMIP5 and the experiment design. Bull Am Meteor Soc 934:485–498. doi:10.1175/BAMS-D-11-00094.1

Timmermann A, Oberhuber J, Bacher A, Esch M, Latif M, Roeckner E (1999) Increased El Nino frequency in a climate model forced by future greenhouse warming. Nature 398:694–697

Timmermann A, Jin F-F, Abshagen J (2003) A nonlinear theory for El Nino bursting. J Atmos Sci 60:152–165

Torrence T, Webster PJ (1998) Interdecadal changes in the ENSO–monsoon system. J Clim 12:2679–2690

Waliser DE, Graham NE (1993) Convective cloud systems and warm-pool sea surface temperatures: coupled interactions and self-regulation. J Geophy Res Atmos 98:12881–12893

Wang B, An S-I (2001) Why the properties of El Nino changed during the late 1970s. Geophys Res Lett 28:3709–3712

Wang B, An S-I (2002) A mechanism for decadal changes of ENSO behavior: roles of background wind changes. Clim Dyn 18:475–486

Wittenberg AT (2009) Are historical records sufficient to constrain ENSO simulations? Geophys Res Lett 36:L12702. doi:10.1029/2009GL038710

Wittenberg AT, Rosati A, Delworth TL, Vecchi GA, Zeng F (2014) ENSO modulation: is it decadally predictable? J Clim. doi:10.1175/JCLI-D-13-00577.1

Yu J-Y, Kim S-T (2010) Identification of central-Pacific and eastern-Pacific types of ENSO in CMIP3 models. Geophys Res Lett 37:L15705. doi:10.1029/2010GL044082

Zebiak SE, Cane M (1987) A model El Nino-Southern oscillation. Mon Weather Rev 115:2262–2278